

Simulation of non-hydrostatic, density-stratified flow in irregular domains

Kraig B. Winters^{a,c,*}, Harvey E. Seim^b and Timothy D. Finnigan^c

^a *Applied Physics Laboratory and Department of Applied Mathematics, University of Washington, Seattle, WA, USA*

^b *Skidaway Institute of Oceanography, Savannah, GA, USA*

^c *Centre for Water Research, University of Western Australia, Nedlands, Western Australia, Australia*

SUMMARY

A numerical model has been developed for simulating density-stratified flow in domains with irregular but simple topography. The model was designed for simulating strong interactions between internal gravity waves and topography, e.g. exchange flows in contracting channels, tidally or convectively driven flow over two-dimensional sills or waves propagating onto a shoaling bed. The model is based on the non-hydrostatic, Boussinesq equations of motion for a continuously stratified fluid in a rotating frame, subject to user-configurable boundary conditions. An orthogonal boundary fitting co-ordinate system is used for the numerical computations, which rely on a fourth-order compact differentiation scheme, a third-order explicit time stepping and a multi-grid based pressure projection algorithm. The numerical techniques are described and a suite of validation studies are presented. The validation studies include a pointwise comparison of numerical simulations with both analytical solutions and laboratory measurements of non-linear solitary wave propagation. Simulation results for flows lacking analytical or laboratory data are analysed *a posteriori* to demonstrate satisfaction of the potential energy balance. Computational results are compared with two-layer hydraulic predictions in the case of exchange flow through a contracting channel. Finally, a simulation of circulation driven by spatially non-uniform surface buoyancy flux in an irregular basin is discussed. Copyright © 2000 John Wiley & Sons, Ltd.

KEY WORDS: density-stratified flow; topography; compact differencing; projection; curvilinear

1. INTRODUCTION

There are many geophysical flows where the interaction of a density-stratified fluid with variable topography is the dynamical effect of primary interest. Hydraulically controlled flow through straits, internal wave generation and propagation near sills, and waves approaching shoaling bathymetry are but a few examples. To study these problems using computational methods is often difficult. To simulate non-linear wave dynamics, the high accuracy and good

* Correspondence to: Department of Environmental Engineering, Centre for Water Research, The University of Western Australia, Nedlands, Western Australia 6907, Australia.

phase properties of (global) spectral methods are desirable but, unfortunately, these methods are inherently limited to simple geometries. There are many codes available that are designed for large-scale simulation of hydrostatic flow in domains intended to represent naturally occurring variability. These codes, however, represent non-linear waves only poorly, both due to the hydrostatic approximation and to the low-order discretizations typically used. A non-hydrostatic numerical model that could be employed in non-uniform domains but based on relatively high-order numerical methods would thus be a useful tool for a reasonably broad class of problems.

Here, such a model is presented, designed for process-oriented simulation studies of density-stratified flow in irregular bathymetries. The purpose of this paper is threefold: to document the underlying numerical techniques, to validate the methodology through a small suite of test cases and to illustrate by example some of the types of flow that can be studied using these techniques. The numerical code is called S-FIT, for stratified-flow interacting with topography.

S-FIT was designed for detailed investigations of idealized flows in irregular but relatively simple domains, where non-uniformities in the geometry occur in two rather than three dimensions. In its simplest configuration, the model is intended for direct numerical simulations (DNS), i.e. it provides approximate solutions to the (non-hydrostatic) Navier–Stokes equations for incompressible, rotating, density-stratified fluids given appropriate initial and boundary conditions. The algorithm relies on a numerically generated transformation from boundary fitting, orthogonal curvilinear co-ordinates to a regularly structured computational grid. This transformation allows the use of accurate, easily coded numerical methods, at the cost of working with the more complicated, transformed equations of motion. Because grid lines intersect the boundaries orthogonally, numerical representation of the relevant boundary conditions poses no particular complication. Boundary conditions are thus treated accurately and consistently with the interior discretizations. The original motivation for developing the model was to simulate flows that are strongly rather than weakly influenced by geometrical variability, and within which, boundary interactions are communicated to the interior flow by means of internal gravity waves.

The numerical methods have been implemented and tested for two geometrical configurations: variable width channels with vertical side-walls and channels or basins with depth variation along one horizontal co-ordinate. The model generates numerical solutions for either unforced initial value problems or for flows forced by surface stress, surface heat transfers or by externally established barotropic pressure gradients. Open boundary conditions with optional damping or viscous fringe regions can also be invoked. Though limited, these configurations permit simulation of a modest range of geophysically motivated stratified flows, e.g.

1. non-linear evolution of basin scale seiching waves;
2. exchange flow through a contracting channel, driven by density and pressure differences between two reservoirs;
3. exchange flow between two basins separated by a sill, driven by laterally variable surface cooling;
4. tidally driven, stratified flow over a two-dimensional sill;

5. plunging inflow to a sloping basin;
6. internal wave breaking over shoaling bathymetry.

The remainder of the paper is organized as follows. The equations of motion, the basic notation and the allowable geometries are described in Section 2, along with the transformation of the equations to curvilinear co-ordinates and the grid generation. The solution techniques are discussed in Section 3 followed by validation comparisons with analytical solutions in Section 4. Sample applications, automatically generated validation diagnostics, and a comparison of simulation results with laboratory measurements and approximate theory are shown in Section 5.

2. EQUATIONS OF MOTION AND ALLOWABLE GEOMETRIES

The equations of motion for an incompressible, density-stratified fluid under the Boussinesq approximation are

$$\frac{\partial}{\partial t} \vec{u} + \vec{u} \cdot \nabla \vec{u} + \hat{z} \times f \vec{u} = -\frac{1}{\rho_0} \nabla p - \hat{z} \frac{g}{\rho_0} \rho' + \nabla \cdot \nu \nabla \vec{u}, \quad (1)$$

$$\frac{\partial}{\partial t} \rho' + \vec{u} \cdot \nabla \rho' + w \frac{d}{dz} \bar{\rho} = \nabla \cdot \kappa \nabla \rho', \quad (2)$$

$$\nabla \cdot \vec{u} = 0. \quad (3)$$

Here, \vec{u} is the velocity vector with components $[u, v, w]$ in the Cartesian co-ordinate directions x, y and z ; ρ' is the density perturbation from an arbitrarily specified, time-independent profile $\bar{\rho}(z)$; ρ_0 is a constant reference density; g is the gravitational acceleration; f is the Coriolis parameter; and \hat{z} is the unit vector in the vertical direction (positive upward). For now, the coefficients ν and κ are regarded as molecular viscosity and diffusivity respectively, with time- and space-independent values; but note that they could be interpreted as eddy coefficients if a subgrid scale model were to be introduced to estimate their values as functions of the resolved scale flow.

2.1. 'Reduced-complexity' domains

The primary interest involves the interaction of internal gravity waves and currents with non-uniform topography. Therefore, approximate solutions to Equations (1)–(3) in irregular domains are desired. Arbitrarily complex geometries in three dimensions can easily lead to computational demands beyond the present capabilities, especially if relatively high-order numerical methods at moderate to high resolution are desired. For this reason, and because there remain many fundamental problems that can be formulated in simpler geometries, the numerical model is designed for application in either of two reduced-complexity domains. The purpose of this type of computation is not to simulate specific flows in specific domains that are realistically represented, but to explore in detail the basic physics and processes characterizing density-stratified flows, which are strongly influenced by topographical variability.

Figure 1 is a schematic of the two allowable geometrical configurations for S-FIT. Each computational domain consists of the volume in space defined by the translation of a simple, closed planar region in the direction normal to the plane itself. The two configurations are distinguished by the orientation direction of the planar regions, i.e. whether the planes lie parallel or perpendicular to the direction of gravity. Domains similar to that in Figure 1(a) are denoted Ω_{xy} and are characterized by simple, closed regions in a horizontal plane. A three-dimensional volume is obtained through vertical translation over a specified distance L . Within the x - y horizontal plane, a curvilinear, boundary fitting co-ordinate system is defined. By requiring the domain shape to be uniform in the z -direction, the x - y curvilinear co-ordinate system can be retained for all z . The resulting computational domain can in this

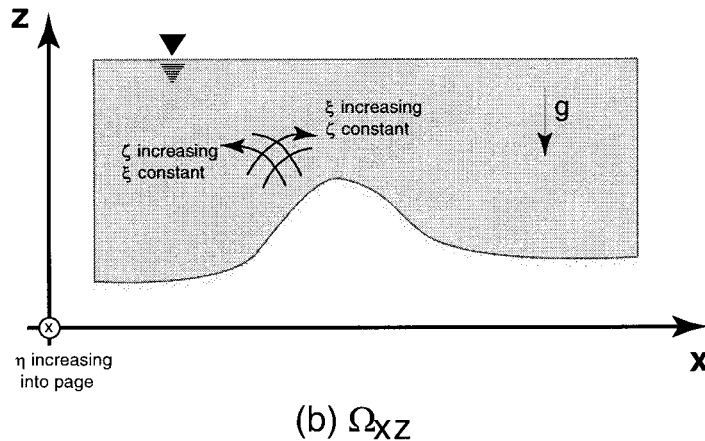
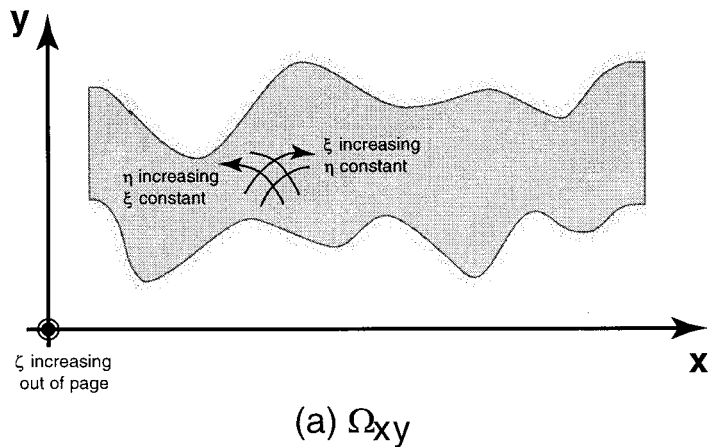


Figure 1. Schematic showing the two allowable domains for the computational model.

sense be regarded as separable. Ω_{xy} domains are appropriate for simulating flow in vertical side-wall channels of constant depth and variable width.

Domains similar to that in Figure 1(b) are denoted Ω_{xz} and differ only in that the closed regions and curvilinear co-ordinates are prescribed in a vertical $x-z$ plane. Translation is then taken laterally (in y) to form the three-dimensional computational space. Ω_{xz} domains are thus appropriate for simulating flow in simple channels with depth variation in one horizontal direction, e.g. hydraulically-controlled flow over two-dimensional sills.

To reduce computational complexity, it is required that the two-dimensional curvilinear co-ordinate systems in either domain to be orthogonal, i.e. to obey $x_\xi y_\xi + x_\eta y_\eta = 0$ in Ω_{xy} or $x_\xi z_\xi + x_\zeta z_\zeta = 0$ in Ω_{xz} . It is convenient to work with velocity vectors oriented along grid lines defined by holding ξ , η or ζ constant and thus introduce the following transformation pairs for the velocity components along the curvilinear grid lines. For Ω_{xy} let

$$\begin{bmatrix} u \\ v \end{bmatrix} = \begin{bmatrix} x_\xi & x_\eta \\ y_\xi & y_\eta \end{bmatrix} \begin{bmatrix} U \\ V \end{bmatrix} \quad \text{and} \quad \begin{bmatrix} U \\ V \end{bmatrix} = \frac{1}{\mathcal{J}_{xy}} \begin{bmatrix} y_\eta & -x_\eta \\ -y_\xi & x_\xi \end{bmatrix} \begin{bmatrix} u \\ v \end{bmatrix}, \quad (4)$$

and similarly for Ω_{xz}

$$\begin{bmatrix} u \\ w \end{bmatrix} = \begin{bmatrix} x_\xi & x_\zeta \\ z_\xi & z_\zeta \end{bmatrix} \begin{bmatrix} U \\ W \end{bmatrix} \quad \text{and} \quad \begin{bmatrix} U \\ W \end{bmatrix} = \frac{1}{\mathcal{J}_{xz}} \begin{bmatrix} z_\zeta & -x_\zeta \\ -z_\xi & x_\xi \end{bmatrix} \begin{bmatrix} u \\ w \end{bmatrix}, \quad (5)$$

where

$$\mathcal{J}_{xy}(\xi, \eta) = x_\xi y_\eta - x_\eta y_\xi \quad \text{and} \quad \mathcal{J}_{xz}(\xi, \zeta) = x_\xi z_\zeta - x_\zeta z_\xi. \quad (6)$$

2.2. Transformed equations of motion

Using these transformations and the differentiation formulae (7) and (8)

$$\begin{bmatrix} f_x \\ f_y \end{bmatrix} = \frac{1}{\mathcal{J}_{xy}} \begin{bmatrix} y_\eta & -y_\xi \\ -x_\eta & x_\xi \end{bmatrix} \begin{bmatrix} f_\xi \\ f_\eta \end{bmatrix}, \quad (7)$$

$$\begin{bmatrix} f_x \\ f_z \end{bmatrix} = \frac{1}{\mathcal{J}_{xz}} \begin{bmatrix} z_\zeta & -z_\xi \\ -x_\zeta & x_\xi \end{bmatrix} \begin{bmatrix} f_\xi \\ f_\zeta \end{bmatrix}, \quad (8)$$

Equations (1)–(3) can be written in terms of the transformed variables. For Ω_{xy} , we have

$$\frac{\partial}{\partial t} U + \alpha_{1,1} U^2 + \alpha_{1,2} UV + \alpha_{1,3} V^2 - \gamma_{xy}^1 fV = -\frac{1}{\rho_0} \mathcal{G}_{xy}^\xi [p] + \text{diss}(U), \quad (9)$$

$$\frac{\partial}{\partial t} V + \alpha_{2,1} U^2 + \alpha_{2,2} UV + \alpha_{2,3} V^2 + \gamma_{xy}^2 fU = -\frac{1}{\rho_0} \mathcal{G}_{xy}^\eta [p] + \text{diss}(V), \quad (10)$$

$$\frac{\partial}{\partial t} w + \frac{g}{\rho_0} \rho' = -\frac{1}{\rho_0} \mathcal{G}_{xy}^\zeta [p] + \text{diss}(w), \tag{11}$$

$$\frac{d}{dt} \rho' + \frac{1}{z_\zeta} w \frac{d}{d\zeta} \bar{\rho} = \text{diff}(\rho), \tag{12}$$

$$\mathcal{D}_{xy}[U, V, w] = \frac{1}{\mathcal{J}_{xy}} \left(\frac{\partial}{\partial \xi} (\mathcal{J}_{xy} U) + \frac{\partial}{\partial \eta} (\mathcal{J}_{xy} V) \right) + \frac{1}{z_\zeta} \frac{\partial}{\partial \zeta} w = 0, \tag{13}$$

$$\frac{d}{dt} \equiv \frac{\partial}{\partial t} + U \frac{\partial}{\partial \xi} + V \frac{\partial}{\partial \eta} + \left(\frac{1}{z_\zeta} \right) w \frac{\partial}{\partial \zeta}, \tag{14}$$

where $\mathcal{G}_{xy}^\xi [p]$ is the ξ component of the vector operator \mathcal{G}_{xy} acting on the pressure p . The variable coefficients $\alpha_{i,j}$ and γ_{xy}^i and \mathcal{G}_{xy} are defined in Table I, and Equation (13) defines the divergence operator \mathcal{D}_{xy} .

Similarly, in the domain Ω_{xz} , we obtain

$$\frac{d}{dt} U + \beta_{1,1} U^2 + \beta_{1,2} UW + \beta_{1,3} W^2 - \frac{x_\zeta}{\mathcal{J}_{xz}} \frac{g}{\rho_0} \rho' - \gamma_{xz}^1 f v = -\frac{1}{\rho_0} \mathcal{G}_{xz}^\xi [p] + \text{diss}(U), \tag{15}$$

$$\frac{d}{dt} v + f(x_\xi U + x_\zeta W) = -\frac{1}{\rho_0} \mathcal{G}_{xz}^\eta [p] + \text{diss}(v), \tag{16}$$

$$\frac{d}{dt} W + \beta_{3,1} U^2 + \beta_{3,2} UW + \beta_{3,3} W^2 + \frac{x_\zeta}{\mathcal{J}_{xz}} \frac{g}{\rho_0} \rho' + \gamma_{xz}^3 f v = -\frac{1}{\rho_0} \mathcal{G}_{xz}^\zeta [p] + \text{diss}(W), \tag{17}$$

$$\frac{d}{dt} \rho' + W \frac{d}{d\zeta} \bar{\rho} = \text{diff}(\rho), \tag{18}$$

$$\mathcal{D}_{xz}[U, v, W] = \frac{1}{\mathcal{J}_{xz}} \left(\frac{\partial}{\partial \xi} (\mathcal{J}_{xz} U) + \frac{\partial}{\partial z} (\mathcal{J}_{xz} W) \right) + \frac{1}{y_\eta} \frac{\partial}{\partial \eta} v = 0, \tag{19}$$

Table I. Coefficients for Ω_{xy} domains

$\alpha_{1,1} = \frac{(y_\eta x_{\xi\xi} - x_\eta y_{\xi\xi})}{\mathcal{J}_{xy}}$	$\alpha_{1,2} = \frac{2(y_\eta x_{\xi\eta} - x_\eta y_{\xi\eta})}{\mathcal{J}_{xy}}$	$\alpha_{1,3} = \frac{(y_\eta x_{\eta\eta} - x_\eta y_{\eta\eta})}{\mathcal{J}_{xy}}$
$\alpha_{2,1} = \frac{(x_\xi y_{\xi\xi} - x_\eta y_{\xi\xi})}{\mathcal{J}_{xy}}$	$\alpha_{2,2} = \frac{2(x_\xi y_{\xi\eta} - y_\xi x_{\xi\eta})}{\mathcal{J}_{xy}}$	$\alpha_{2,3} = \frac{(x_\xi y_{\eta\eta} - y_\xi x_{\eta\eta})}{\mathcal{J}_{xy}}$
$\gamma_{xy}^1 = \frac{x_\eta^2 + y_\eta^2}{\mathcal{J}_{xy}}$	$\gamma_{xy}^2 = \frac{x_\xi^2 + y_\xi^2}{\mathcal{J}_{xy}}$	NA
$\mathcal{G}_{xy}^\xi = \frac{(x_\eta^2 + y_\eta^2)}{\mathcal{J}_{xy}^2} p_\xi$	$\mathcal{G}_{xy}^\eta = \frac{(x_\xi^2 + y_\xi^2)}{\mathcal{J}_{xy}^2} p_\eta$	$\mathcal{G}_{xy}^\zeta = z_\zeta p_\zeta$

$$\frac{d}{dt} \equiv \frac{\partial}{\partial t} + U \frac{\partial}{\partial \xi} + \left(\frac{1}{y_\eta} \right) v \frac{\partial}{\partial \eta} + W \frac{\partial}{\partial \zeta}, \quad (20)$$

where, for example, $\mathcal{G}_{xz}^\zeta[p]$ is the ζ component of $\mathcal{G}_{xz}[p]$, defined in Table II along with the coefficients β_{ij} and γ_{xz}^i . For both sets of equations, the notation ‘diss’ and ‘diff’ represent transformation of the dissipation and diffusion terms respectively, allowing for the possibility of spatially varying coefficients ν and κ . Although more complicated than in their original forms, the transformed equations are much simpler than those for more general three-dimensional curvilinear co-ordinates. The restriction to the simpler domains Ω_{xy} and Ω_{xz} limits the spatial variability of α_{ij} , β_{ij} and γ_{ij} , as well as the non-constant coefficients associated with the \mathcal{G} and \mathcal{D} operators to two dimensions. This results in a large saving in computer memory, which makes the overall solution algorithm computationally feasible. The restriction to orthogonal co-ordinates further simplifies the equations somewhat by reducing the number of non-linear velocity products that appear. Finally, the combination of boundary orthogonality and grid-aligned velocity components greatly simplifies the form of dynamically relevant boundary conditions.

2.3. Orthogonal grid generation

The construction of a network of grid lines that intersect orthogonally and are coincident with specified boundary curves (see Figure 1) is accomplished using the covariant Laplace equation method [1,2]. It is noted that, aside from the notation, the grid generation procedure is identical for both domains Ω_{xy} and Ω_{xz} , and thus the method is described using the notation appropriate for Ω_{xy} . The computational mesh is defined as a set of regularly spaced grid points (ξ_{ij}, η_{ij}) for $i = 1, 2, \dots, N_\xi$ and $j = 1, 2, \dots, N_\eta$ with $0 \leq \xi \leq L_\xi$ and $0 \leq \eta \leq L_\eta$. The co-ordinate transformation represents a mapping from the set of computational grid points (ξ_{ij}, η_{ij}) to a discrete set of spatial locations (x_{ij}, y_{ij}) , which sample a dense set of orthogonal, curvilinear grid lines. For a specified boundary geometry, the mapping is obtained via the numerical solution of three successive elliptic boundary value problems. In the covariant Laplace method, three constraints are imposed on the co-ordinate map, namely

Table II. Coefficients for Ω_{xz} Domains

$\beta_{1,1} = \frac{(z_\zeta x_{\xi\xi} - x_\zeta z_{\xi\xi})}{\mathcal{J}_{xz}}$	$\beta_{1,2} = \frac{2(z_\zeta x_{\xi\xi} - x_\zeta z_{\xi\xi})}{\mathcal{J}_{xz}}$	$\beta_{1,3} = \frac{(z_\zeta x_{\xi\xi} - x_\zeta z_{\xi\xi})}{\mathcal{J}_{xz}}$
$\beta_{3,1} = \frac{(x_\xi x_{\xi\xi} - x_\xi z_{\xi\xi})}{\mathcal{J}_{xz}}$	$\beta_{3,2} = \frac{2(x_\xi z_{\xi\xi} - z_\xi x_{\xi\xi})}{\mathcal{J}_{xz}}$	$\beta_{3,3} = \frac{(x_\xi z_{\xi\xi} - z_\xi x_{\xi\xi})}{\mathcal{J}_{xz}}$
$\gamma_{xz}^1 = \frac{z_\zeta}{\mathcal{J}_{xz}}$	NA	$\gamma_{xz}^3 = \frac{z_\xi}{\mathcal{J}_{xz}}$
$\mathcal{G}_{xz}^\xi = \frac{(x_\xi^2 + z_\xi^2)}{\mathcal{J}_{xz}^2} p_\xi$	$\mathcal{G}_{xz}^\eta = y_\eta p_\eta$	$\mathcal{G}_{xz}^\zeta = \frac{(x_\xi^2 + z_\xi^2)}{\mathcal{J}_{xz}^2} p_\zeta$

- edge points of the computational mesh are mapped to discrete points on the boundary segments defining the non-uniform domain;
- the distributions of discrete boundary points along two of the four segments are prescribed;
- the co-ordinate lines are orthogonal in the physical (x, y) domain.

The first constraint is clearly necessary for all simple grids. By prescribing the distribution of boundary points, the spatial distribution of the grid resolution can be controlled. Although specification of boundary correspondence on two sides was found to be adequate for purposes here, Oh and Kang [3] have shown that correspondence can be specified on up to three sides. Because we only require the grid generation to be done once, prior to the flow simulations, the implementation of the covariant Laplace technique employs accurate numerical techniques wherever possible. For example, the singularities in the integral equations arising in the boundary integral method are first removed analytically, leaving a residual integration that is estimated numerically to fourth-order accuracy. This is done generally; no geometry specific analysis is required. Discrete derivative operators, as well as the interior elliptic solver are also fourth-order-accurate. Furthermore, the intermediate, conformal mapping calculations are performed using a finer discretization than that of the final grid mapping.

Figure 2 shows the grid lines used for the exchange flow example discussed in Section 7.2. After the grid was constructed, the magnitude of the intersection angles, θ , where

$$\cos \theta(\xi, \eta) = \frac{x_\xi x_\eta + y_\xi y_\eta}{(x_\xi^2 + y_\xi^2)^{1/2} (x_\eta^2 + y_\eta^2)^{1/2}}, \quad (21)$$

and were determined by numerical differentiation of $x(\xi, \eta)$ and $y(\xi, \eta)$ using a fourth-order compact differencing scheme [4]. The average deviation from orthogonality for the grid shown in Figure 2 is 6×10^{-5} rad.

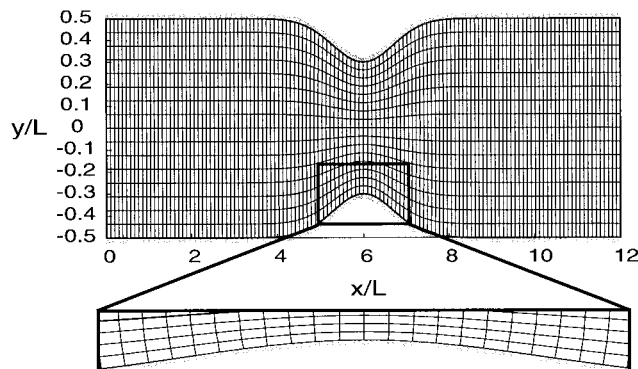


Figure 2. Plan view of non-uniform channel and curvilinear grid.

3. SOLUTION OF THE TRANSFORMED EQUATIONS

Before describing the numerical methods, it is convenient to rewrite Equations (9)–(19) as

$$\frac{\partial}{\partial t} \vec{U} = \vec{\mathcal{F}}_u - \frac{1}{\rho_0} \mathcal{G}[p], \quad (22)$$

$$\frac{\partial}{\partial t} \rho' = \mathcal{F}_\rho, \quad (23)$$

$$\mathcal{D}[\vec{U}] = 0, \quad (24)$$

where the vector \vec{U} is understood to have components $[U, V, w]$ in Ω_{xy} , and $[U, v, W]$ in Ω_{xz} , and the operators \mathcal{G} and \mathcal{D} take their respective forms in the two domains. The terms $\vec{\mathcal{F}}_u$ and \mathcal{F}_ρ are then defined by the correspondence between (9)–(13) or (15)–(19) and (22)–(24) in Ω_{xy} or Ω_{xz} respectively.

Time integration of these equations is carried out in two stages. Assuming the velocity and density fields are known at time t and the solutions are desired at time $t + \Delta t$, an intermediate velocity vector \vec{U}_* is first defined, where

$$\vec{U}_*(\xi, \eta, \zeta) = \vec{U}(\xi, \eta, \zeta, t) + \int_t^{t+\Delta t} \vec{\mathcal{F}}_u dt. \quad (25)$$

Introducing the function P such that

$$\vec{U}(\xi, \eta, \zeta, t + \Delta t) = \vec{U}_* - \frac{\Delta t}{\rho_0} \mathcal{G}[P], \quad (26)$$

it follows, for example, that

$$\frac{\Delta t}{\rho_0} \mathcal{G}_{xy}^\xi[P] = \frac{1}{\rho_0} \int_t^{t+\Delta t} \mathcal{G}_{xy}^\xi[p] dt, \quad (27)$$

and hence

$$P_\xi = \frac{1}{\Delta t} \int_t^{t+\Delta t} p_\xi dt. \quad (28)$$

Similar expressions are obtained for P_η and P_ζ in both domains. Note that derivatives of the introduced function P are related to those of fluid pressure p through a time average over the time interval Δt .

An elliptic equation for P is obtained by applying the appropriate form of \mathcal{D} to Equation (26) and imposing the appropriate condition of incompressibility, Equation (13) or (19), on $\vec{U}(\xi, \eta, \zeta, t + \Delta t)$,

$$\mathcal{D}[\mathcal{G}[P]] = -\frac{\rho_0}{\Delta t} \mathcal{D}[\vec{U}_*]. \quad (29)$$

Recalling the definitions of \mathcal{D} and \mathcal{G} , it is seen that Equation (29) is a linear second-order elliptic equation with mixed derivative terms and spatially variable, but time-independent, coefficients. The source term depends on the values of \vec{U}_* and thus varies in both space and time. Two types of boundary conditions are required in order to fully specify P . At solid walls, the values of the normal derivatives, $\partial P/\partial \eta$, are determined by resolving Equation (26) into the directions normal to the walls and imposing zero values for the normal velocities. At open boundaries, for example, in cases where the up- and downstream computational boundaries do not correspond with physical boundaries, the exact boundary conditions for pressure are unknown, i.e. mathematically underdetermined. In an attempt to prescribe radiating 'open' boundary conditions, the pressure has been specified to be hydrostatic on these vertical planes. In practice, damping or fringe regions adjacent to open boundaries are specified to minimize unwanted reflections.

3.1. Numerical implementation

Given the velocity field \vec{U} and the density field ρ' at discrete grid points at time t^n , the numerical procedure to estimate the solutions at time $t^{n+1} = t^n + \Delta t$ consists of the following steps:

(1) Calculate the intermediate velocity field \vec{U}_* and the t^{n+1} density field ρ'^{n+1} using the third-order Adams–Bashforth time integration scheme

$$\vec{U}_*^{n+1} = \vec{U}^n + \frac{\Delta t}{12} [23\mathcal{F}_u^n - 16\mathcal{F}_u^{n-1} + 5\mathcal{F}_u^{n-2}], \quad (30)$$

$$\rho'^{n+1} = \rho'^n + \frac{\Delta t}{12} [23\mathcal{F}_\rho^n - 16\mathcal{F}_\rho^{n-1} + 5\mathcal{F}_\rho^{n-2}]. \quad (31)$$

Note that previously computed values of the function \mathcal{F} must be stored in order to carry out the updates and that lower-order start-up schemes are required for the first two time steps. The spatial derivatives required to evaluate the function \mathcal{F} are estimated using a fourth-order compact scheme [4,5].

(2) Given the intermediate velocity field \vec{U}_* , calculate $\mathcal{D}[\vec{U}_*]$ using the same compact scheme for spatial derivatives. The precise forms of \mathcal{D} and \vec{U} depend on the choice of domains.

(3) Solve Equation (29) for P to fourth-order spatial accuracy. Here, MUDPACK [6,7], a multi-grid solver for linear second-order elliptic equations in three dimensions is used.

(4) Calculate $\mathcal{G}[P]$, again using fourth-order compact differentiation, and update the intermediate velocity \vec{U} as specified in Equation (26).

(5) Low-pass filter the solutions to eliminate growth of numerical instabilities at the smallest scales. Filtering smoothes the solutions over scales slightly larger than the grid resolution. A fourth-order compact filtering scheme [5], with filtering parameter $\alpha = 0.475$, is applied every j th time step, where j is a user-specified parameter.

4. VALIDATION SIMULATIONS

As with any numerical code, it is necessary to develop confidence in the implementation and methodology through validation studies. A validation strategy has been designed, which consists of checks at several levels.

1. Quantitative testing against simple flows in simple domains with known analytical solutions.
2. Quantitative testing against physical measurement in the laboratory.
3. Automatic checking of global constraints, i.e. incompressibility and satisfaction of the potential energy balance.
4. Qualitative examination of solutions for more complicated flows in irregular domains and comparison with approximate theory where possible.

Any one of these checks would be incomplete. Application of the ensemble of tests, however, provides reasonable assurance that the numerical algorithms are properly implemented.

4.1. Scalar diffusion

The analytical solution of the heat equation can be used to test the time stepping and the spatial differentiation routines. An exact error function solution describes the diffusion of a scalar from an initially discontinuous state. Smooth initial conditions were created by evaluating the exact solution after some finite time interval. These conditions were then integrated forward in time using the numerical model, comparing the computed values with the exact solution. Tests were made for the diffusion of both momentum and density in each direction. The momentum tests require open or periodic boundary conditions to be specified in the streamwise direction and free-slip or zero stress conditions at the other boundaries.

Figure 3 shows the computed and exact solution given by Equation (32),

$$u(z, t) = \frac{U}{2} - \frac{U}{2} \operatorname{erf} \left[\frac{(z - z_0)}{(4\nu t)^{1/2}} \right], \quad (32)$$

for diffusion of horizontal momentum in the vertical direction. The analytical solution is formally valid in an infinite domain. Differences between the computed and analytical solutions are to be expected once the diffusive signal approaches the boundaries in a finite domain. To assess solution quality, the root-mean-square (r.m.s.) relative error was computed for $\frac{1}{4} < z < \frac{3}{4}$ at $t = 12$ s for several values of dz using the same time step dt . The errors are always small and decrease with increasing spatial resolution as expected. The figure shows the temporal evolution with 65 grid points in the vertical.

4.2. Time-dependent Couette flow

Simulation of the development of plane Couette flow exercises the numerical treatment of inhomogeneous boundary conditions. Equation (33) is a series expansion for flow resulting from viscous stress at a rigid boundary moving at speed U_0 [8].

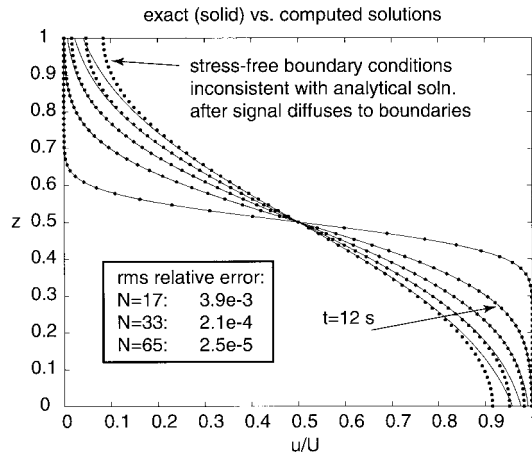


Figure 3. Comparison of computed and exact solutions for diffusion of momentum.

$$\frac{u}{U_0} = \left(1 - \frac{z}{h}\right) - \frac{2}{\pi} \sum_{n=1}^{\infty} \frac{1}{n} \exp(-n^2 \pi^2 \nu t / h^2) \sin \frac{n\pi z}{h}. \tag{33}$$

Figure 4 shows the comparison between the converged series solution and the simulated flow on a relatively coarse grid of 33 vertical grid points at several instants in time. The agreement is excellent with typical r.m.s. relative errors of $O(10^{-4})$, independent of the time step provided dt is less than about 0.1.

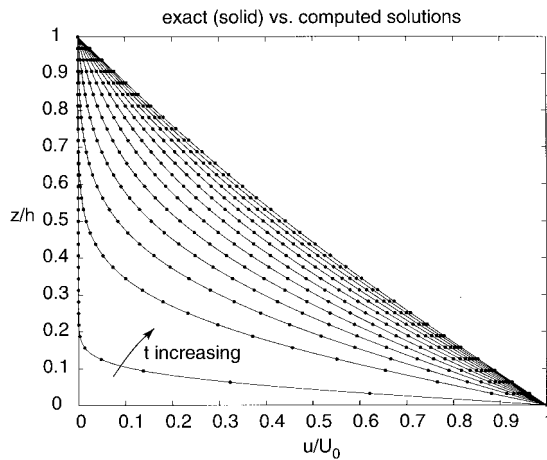


Figure 4. Comparison of computed and exact solutions for plane Couette flow.

4.3. Internal gravity waves

Exact solutions for linear internal gravity waves are valid in the limit of vanishing viscosity and diffusivity for small amplitude disturbances. These cases test the treatment of the baroclinic forces and the rotation terms. For constant background stratification, velocity and density perturbations are simple sinusoids in space and time with an oscillation frequency ω determined by the dispersion relation,

$$\omega^2 = \frac{(k^2 + l^2)N^2 + m^2f^2}{(k^2 + l^2 + m^2)}. \quad (34)$$

Here k and l are the horizontal wavenumbers, m is the vertical wavenumber, N is the buoyancy frequency and f is the Coriolis parameter.

Figures 5 and 6 show the comparison between computed and exact solutions for a mode (3, 2, 1) wave (in the (x, y, z) directions) in a laterally periodic cube with stress-free upper and lower lids.

Additional simulations were run with $f = 0$. For finite amplitude waves, the non-linear terms in the equations of motion are non-zero individually but sum to zero in each equation, i.e. finite amplitude internal waves in a non-rotating frame have zero helicity and hence obey linear internal wave equations. These simulations thus provide a partial test of the non-linear terms. Errors in the treatment of the non-linear terms would produce non-vanishing non-linear effects, and hence a deviation from the linear solution. Several cases were tested with good agreement in each instance.

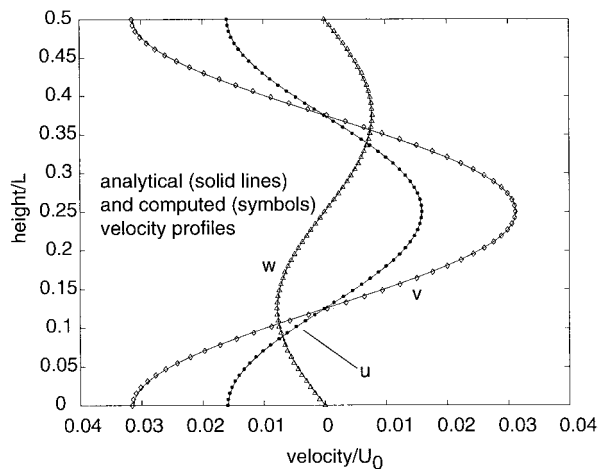


Figure 5. Comparison of simulated and measured instantaneous velocity profiles at a fixed (x, y) location for small amplitude internal gravity waves in a rotating frame.

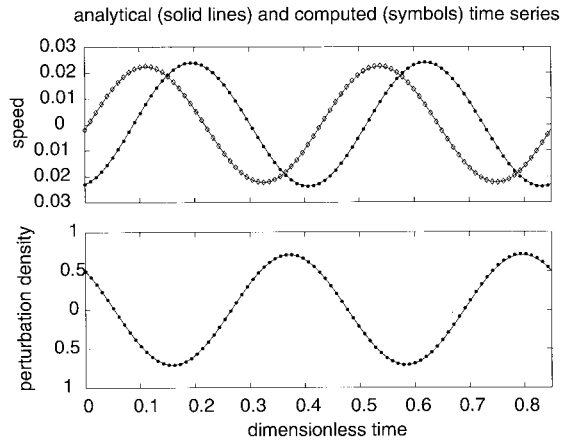


Figure 6. Comparison of simulated and measured velocity and perturbation density time series for small amplitude internal gravity waves in a rotating frame.

These tests suggest that the numerical algorithms have been properly implemented. Additional simulations, i.e. for flows lacking exact analytical solutions, are required, however, to further validate the non-linear terms as well as the implementation of the non-uniform geometrical coefficients.

5. SAMPLE APPLICATIONS

In this section, a series of sample applications are presented. These simulations were chosen both to illustrate the types of flows amenable to study and to provide additional validation tests. For these flows, no exact solutions are known and we rely on laboratory measurements, approximate theory and internal consistency diagnostics to assess the model performance.

5.1. Solitary waves in a tilting tank

Here, the results of a numerical simulation are compared with a laboratory experiment of a basin-scale seiching wave degenerating into a train of propagating solitary waves.

An initially tilted, relatively thin thermocline was allowed to relax in an experiment conducted with salt-stratified water in a $6 \times 0.3 \times 0.29$ m³ sealed tank [Horn, Imberger and Ivey, 'The degeneration of basin-scale internal waves in lakes', submitted to *J. Fluid Mech.* (1998)]. The early evolution of the resulting flow is characterized by a nearly linear, basin-scale seiching motion. Energy is quickly transferred to smaller scales through non-linear interaction and the flow at later times is dominated by a dispersing group of amplitude-ordered, internal solitary waves. Two ultrasonic wave gauges recorded the average sound speed over finite vertical intervals at two fixed horizontal locations. From these measurements, instantaneous, vertical averages of density were inferred and compared with numerically computed values.

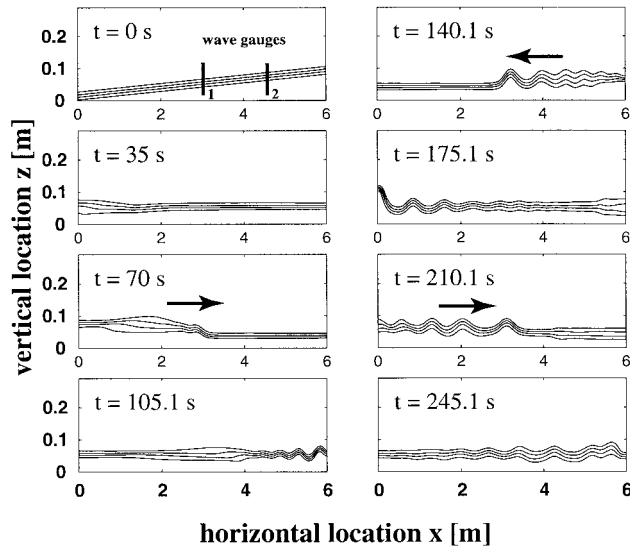


Figure 7. Simulated isopycnals in a vertical plane. The simulation was configured to match a laboratory experiment in a tilting tank. The locations of the two ultrasonic wave gauges are shown.

Figure 7 shows the overall evolution of the wave field and the positions of the wave gauges. Figure 8 shows the comparison of the simulated and measured gauge data. The degeneration of the large-scale mode and the emergence of the solitary wave group are captured remarkably well. For later times, the laboratory and numerical experiments diverge, particularly with respect to phase. The observed differences are consistent with the notion that the numerical

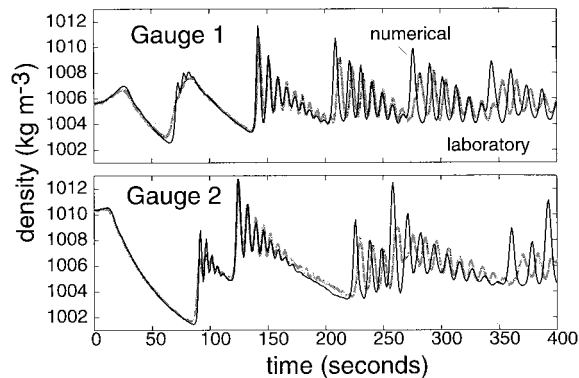


Figure 8. Comparison of simulated and measured wave gauge data.

experiment was run at slightly higher energy than the laboratory experiment. A suite of laboratory runs (Horn *et al.*, submitted) has shown that the non-linearity of the solitary waves is very sensitive to both the relative position (with respect to the upper and lower boundaries) of the equilibrium density interface and the initial angle of tilt. The imprecision in estimating these parameters, which are used in computing the synthetic initial conditions for the numerical experiment, are significant (1 mm and 0.02°) and, we believe, large enough to explain the observed discrepancies. An additional small effect may be due to differences in the Prandtl number $Pr = \nu/\kappa$. The simulations were run with a value of 50 rather than the physical value of 700 for salt-stratified water.

5.2. Exchange flow through a contracting channel

This example tests the implementation of the geometric terms in Ω_{xy} and illustrates the use of the automatic diagnostics verifying incompressibility and potential energy balance.

Exchange flows in which fluids of differing densities flow in opposing directions through a channel are of practical interest in oceanography because of their wide-spread occurrence. Well-known examples occur in the Straits of Gibraltar [9], and the Bosphorus [10], in estuaries [11], and in deep ocean passes [12]. Although analytical solutions for this problem do not exist, approximate solutions have been derived for steady, inviscid, layered flow through a channel [13]. The applicability of the solutions to time-dependent, viscous, continuously stratified systems is an open question. In particular, the existing theory provides no guidance on the role of dissipation, mixing and entrainment across the interface.

To study aspects of exchange flow inaccessible to hydraulic theory, the model was configured to simulate a lock-exchange problem. An open-ended channel with a minimum width near its mid-point is initialized with dense fluid filling one half of the channel, and light fluid filling the other, all at rest. At $t=0$, the fluid begins to adjust, driven by the baroclinic pressure gradient associated with the density contrast, and by an imposed barotropic pressure drop that models a difference in free-surface height between the channel end-points within the rigid-lid formulation. By varying the magnitude of the barotropic pressure difference, the direction and magnitude of the depth-averaged flow can be controlled. The simulated flow evolves to a quasi-steady state in which the interface position is similar to the theoretical prediction (Figure 9).

The principal distinction between theory and the simulation is the finite thickness of the interface, which is seen to vary systematically as a function of along-channel position. This third layer is created by mixing at the interface [14]. The simulations also show higher-order dynamics not captured by the theory, e.g. the generation and propagation of non-hydrostatic waves and shear instabilities.

The lock-exchange calculations are run as large eddy simulations (LES) using a Smagorinsky-like closure scheme to represent subgrid scale processes. In this scheme, vertical viscosities and diffusivities vary in space and time and are determined by the grid-scale shear and stratification, assuming a production/dissipation balance at unresolved scales [15,16]. In this calculation, viscous fringe layers were also employed near the open boundaries to suppress high-wavenumber fluctuations and wave reflections.

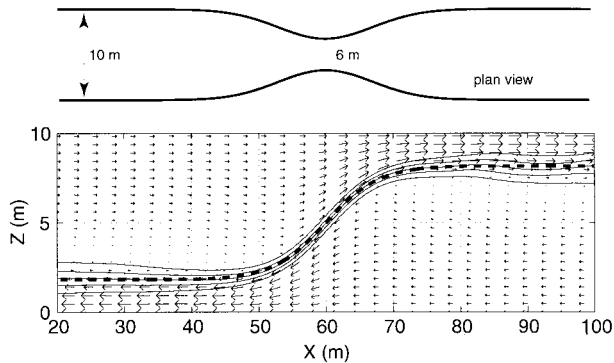


Figure 9. Upper panel: channel geometry. Lower panel: contours of the density field, overlaid with velocity arrows and the predicted position of interface (thick line), of the laterally-averaged fields in an exchange flow. This snapshot is from hour 2 of a nearly-steady simulation with approximately zero depth-averaged flow.

Two diagnostics are routinely computed as the code executes. The first is based on the potential energy equation (35) [17],

$$\frac{d}{dt} E_p = \frac{g}{\rho_0 V} \int_V \rho w \, dV + \frac{g}{\rho_0 V} \oint z \rho \vec{u} \cdot \hat{n} \, dS + \frac{g}{\rho_0 V} \int_V z \nabla \cdot \kappa \nabla \rho \, dV, \quad (35)$$

where

$$E_p = \frac{1}{\rho_0 V} g \int \rho z \, dV. \quad (36)$$

Given the computed solutions at discrete time intervals, generally much larger than the computational time step, the amount by which the potential energy equation does not balance can be estimated, independent of the calculations used to advance the solutions in time. Figure 10 shows the balance over a 10 min interval bounding the time corresponding to Figure 9. The residual has a mean of $5.2 \times 10^{-9} \text{ W kg}^{-1}$ (standard deviation $5.6 \times 10^{-8} \text{ W kg}^{-1}$), which is small compared with the characteristic magnitudes of either the buoyancy flux, the advective flux of potential energy (both approximately $1 \times 10^{-6} \text{ W kg}^{-1}$) or the rate of pressure work ($\approx 1 \times 10^{-5} \text{ W kg}^{-1}$, not shown).

A second diagnostic monitors the overall effectiveness of the pressure solver. One interpretation of the numerically computed field P is that its 'gradient' $\mathcal{G}[P]$ is exactly that field required to project the intermediate solution \vec{U}_* onto its divergence-free subspace. An exact solution for P would identically eliminate divergence while approximate solutions will leave a small residual divergence in the computed flow field. The magnitude of this residual is thus a sensitive diagnostic for the projection scheme as a whole. The magnitude of the volume-averaged divergence is automatically tabulated as the code executes. Typical values for this simulation

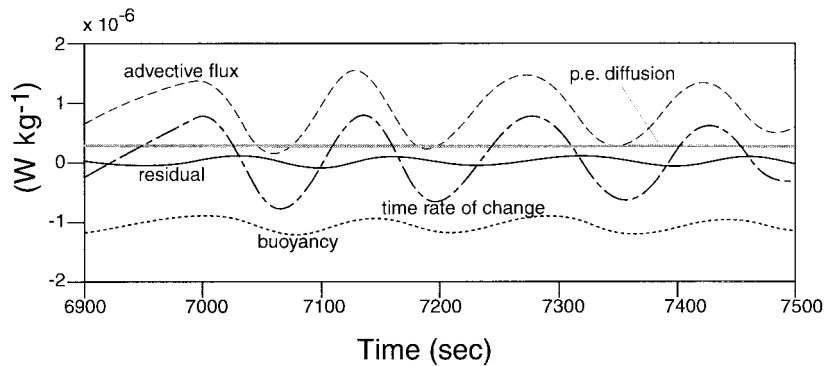


Figure 10. Terms in the potential energy (p.e.) balance equation over a 10 min interval. The terms are (from bottom to top): buoyancy (short dash), residual (solid), p.e. diffusion (grey thick), $\partial/\partial t(\text{p.e.})$ (dash-dot), and advective flux of p.e. (dash).

are of order 10^{-6} s^{-1} , which are small compared with characteristic (inverse) time scales of the physical problem.

5.3. Buoyancy-driven circulation

Two final examples demonstrate proper treatment of the geometrical factors in Ω_{xz} . Figure 11 shows a cross-section of the domain along with the grid lines in the x - z plane. A constant density fluid, initially at rest, is subjected to a negative buoyancy flux B over a portion of the

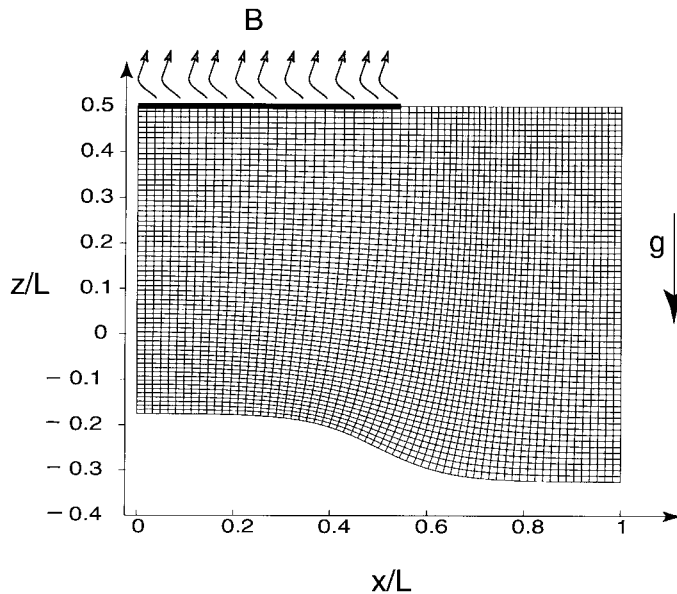


Figure 11. Numerical grid in the x - z plane for simulation of buoyancy driven flow. The region of imposed surface buoyancy flux is indicated.

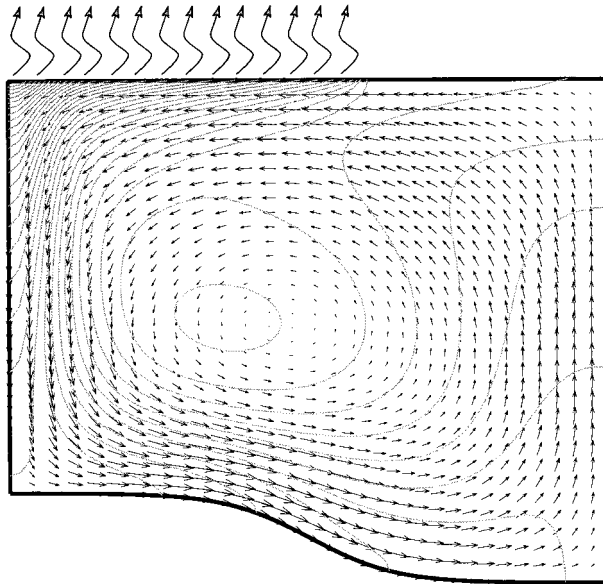


Figure 12. Contours of density and velocity arrows for buoyancy driven circulation at $Ra = 10^6$.

upper surface S_B . A buoyancy-driven circulation is produced, which approaches steady state as $t \rightarrow \infty$. The circulation is similar to that produced in a domain of rectangular cross-section but modified by the presence of the sloping boundary.

Figure 12 shows the instantaneous density contours and a subsampling of the $u-w$ velocity arrows for a simulation with $Ra = g/(\rho_0 \nu \kappa) |d\rho/dz| L^4 = 10^6$. Here L is taken as the nominal vertical scale (see Figure 11) and $|d\rho/dz|$ is the magnitude of prescribed flux over S_B . The snapshot shown was taken from the central vertical plane after the flow had become nearly steady. The flow was computed using a grid mesh of $65 \times 9 \times 65$ points in the ξ -, η - and ζ -directions respectively. For this run, free-slip boundary conditions were imposed at all walls and adiabatic or zero flux conditions were used for density at all boundary points except within the forcing region S_B . Estimated errors in the kinetic and potential energy balances were small, consistent with uncertainty in the assessment of volume integrated kinetic and potential energy in the fourth and fifth significant digit respectively.

5.4. Wave-boundary interaction

The last example illustrates a flow that is characterized primarily by large-scale motions except near a particular spatial location. Here, a large-scale internal wave approaches a sloping boundary where non-linear interactions produce much smaller scales of motion. The ambient stratification has a three-layer structure, with two homogeneous layers separated by a relatively thin pycnocline. A sharp depression of the pycnocline, with finite lateral extent near the right end of the domain, was used as an initial condition. The ensuing flow is a

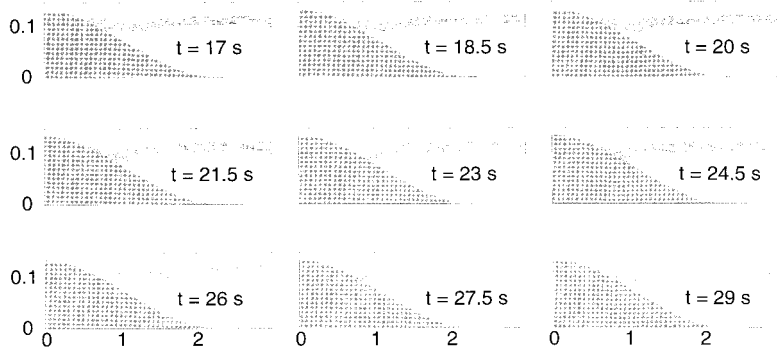


Figure 13. contours of density as a wave of depression approaches a sloping boundary.

leftward propagating wave of depression. Figure 13 shows the cross-sectional shape of the domain and the temporal evolution of the isopycnals as the wave approaches the sloping boundary. The geometry is such that the grid lines focus and the resolution is highest near the region where the wave–boundary interaction occurs. The figure shown is from a relatively low-resolution ($65 \times 9 \times 65$) simulation with grid points in the along-slope, cross-slope and vertical directions respectively.

Figure 14 shows the wave–boundary interaction in more detail at $t = 26$ s. The simulation clearly shows a convergence of up- and down-slope velocity jets as the wave steepens locally, a prominent feature observed in the experiments of Michallet and Ivey [18] using dye and particle image velocimetry (PIV) techniques.

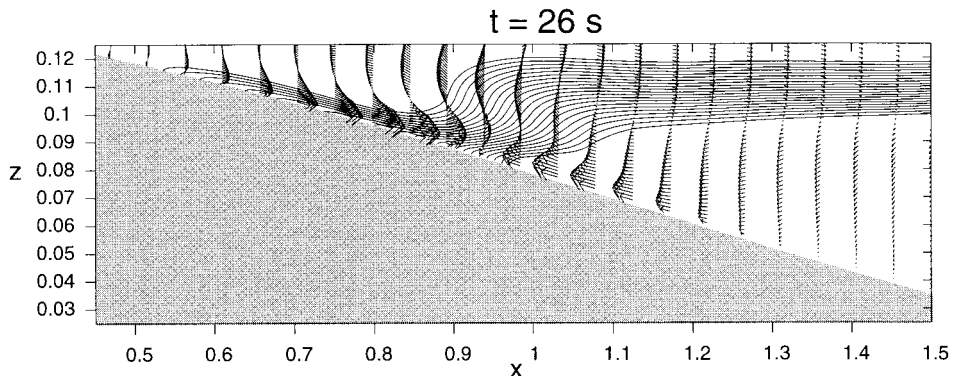


Figure 14. Detail of wave–boundary interaction at $t = 26$ s.

6. DISCUSSION

In conjunction with a boundary-fitting, orthogonal co-ordinate system, a numerical model for simulating three-dimensional, non-hydrostatic flow in irregular domains has been designed and implemented. The implementation and performance of the code have been validated by tests against analytical solutions, laboratory experiments and by internal consistency checks and diagnostics. The primary purpose of the algorithm is for studying idealized flows characterized by waves or buoyancy-induced currents interacting with non-uniform topography. Application of the model is limited to spatial domains with variability in two rather than three dimensions, i.e. the 'reduced complexity' domains described in Section 2. The model is thus designed for the class of problems somewhere between those amenable to the neglect of boundary variability and global spectral methods and those in such complex geometries that severe simplification of the physics and/or low-order numerical methods are required.

Several geophysically motivated example simulations, including an initial value problem for non-linear gravity waves, an exchange flow through a contracting channel, buoyancy-driven flow in a variable depth basin, and waves at a sloping boundary were presented.

The choice of numerical methods reflects a compromise between the high accuracy achievable in undeformed domains and the low-order accuracy necessary for true 'simulation' of naturally occurring flow in complicated bathymetries. The methodology is based on fourth-order compact differencing for spatial derivatives. When combined with the variable transformations, this allows inhomogeneous external conditions over irregular geometries to be treated with relative ease. The pressure projection scheme uses a fourth-order finite difference based multi-grid method to ensure incompressibility of the computed solution. Optionally, this solution can be iteratively refined using a consistent, compact representation of the differential operator but this has not been found to be necessary.

The time stepping scheme is third-order accurate and explicit. In general, explicit treatment of the viscous and diffusive terms restricts the allowable time step due to stability considerations. In practice, however, we have observed that stability requirements associated with advection or internal wave motion are often more stringent than those associated with diffusion. Thus, explicit temporal integration appears not to be a serious limitation, at least for many problems of interest. Furthermore, when feasible, explicit treatment of the viscous terms significantly simplifies the imposition of accurate boundary conditions in the projection scheme relative to implicit methods, see e.g. [19].

At low to moderate Reynolds numbers, DNS simulations may be appropriate. At higher Reynolds numbers, LES via subgrid-scale closure is required. Probably the most significant limitation of the model in its present state is the lack of quantitative confidence in the closure scheme. It is noted, however, that the code has been implemented in terms of spatially and temporally variable eddy viscosity and diffusivity. For DNS simulations, these coefficients are fixed at molecular values and sufficient grid density is necessary to resolve the dissipative scales. When the LES mode is selected, the values of these coefficients are determined using a density-stratified formulation of the Smagorinsky scheme. Substitution of alternative local closure schemes requires the replacement of a single subroutine. We have not yet implemented schemes requiring additional evolution equations, i.e. for turbulent kinetic energy or density variance. Turbulence closure in stratified fluids, particularly when internal waves are important

energy sources for the turbulence, is an active area of current research. An experimental program, perhaps focused on flows similar to the idealized examples presented here, would be useful in helping to evaluate and improve candidate schemes.

ACKNOWLEDGMENTS

This work was supported by the US Office of Naval Research (Code 322, Physical Oceanography) under grants N00014-92-J-1180 and N00014-96-1-0616. The laboratory measurements were made available by David Horn, for which the authors are grateful. They also appreciate the many discussions with Ben Hodges. Computational resources were provided by the Multi-Discipline Group at the University of Washington Applied Physics Laboratory, the Skidaway Institute of Oceanography and the Centre for Water Research, The University of Western Australia.

REFERENCES

1. G. Ryskin and L.G. Leal, 'Orthogonal mapping', *J. Comput. Phys.*, **50**, 71–100 (1983).
2. I.S. Kang and L.G. Leal, 'Orthogonal grid generation in a 2D domain via the boundary integral technique', *J. Comput. Phys.*, **102**, 78–87 (1992).
3. H.J. Oh and I.S. Kang, 'A non-iterative scheme for orthogonal grid generation with control function and specified boundary correspondence on three sides', *J. Comput. Phys.*, **112**, 138–148 (1994).
4. S.K. Lele, 'Compact finite difference schemes with spectral-like resolution', *J. Comput. Phys.*, **103**, 16–42 (1992).
5. D.N. Slinn, 'Numerical simulation of turbulent mixing caused by internal wave reflection from sloping boundaries', *Ph.D Thesis*, University of Washington, 1995.
6. J. Adams, 'MUDPACK: multigrid Fortran software for the efficient solution of linear elliptic partial differential equations', *Appl. Math. Comput.*, **34**, 113–146 (1989).
7. J. Adams, 'Recent enhancements in MUDPACK: a multigrid software package for elliptic partial differential equations', *Appl. Math. Comput.*, **43**, 79–94 (1991).
8. F.M. White, *Viscous Fluid Flow*, 2nd edn., McGraw-Hill, New York, 1991.
9. D.M. Farmer and L. Armi, 'Maximal two-layer exchange over a sill and through the combination of a sill and contraction with barotropic flow', *J. Fluid Mech.*, **164**, 53–76 (1986).
10. T. Oğuz, E. Özsoy, M. Latif, H.I. Sur and U. Ünlüata, 'Modelling of hydraulically controlled exchange flow in the Bosphorus Strait', *J. Phys. Oceanogr.*, **20**, 945–965 (1990).
11. W.R. Geyer and D.M. Farmer, 'Tide-induced variation of the dynamics of a salt wedge estuary', *J. Phys. Oceanogr.*, **19**, 1060–1072 (1989).
12. N.G. Hogg, 'Hydraulic control and flow separation in a multi-layered fluid with applications to the Vema Channel', *J. Phys. Oceanogr.*, **13**, 695–702 (1983).
13. L. Armi and D.M. Farmer, 'The flow of Mediterranean water through the Strait of Gibraltar', *Prog. Oceanogr.*, **21**, 1–105 (1988).
14. K.B. Winters and H.E. Seim, 'The role of dissipation and mixing in an exchange flow through a contracting channel', *J. Fluid Mech.* (2000) in press.
15. D.A. Siegel and J.A. Domaradzki, 'Large eddy simulation of decaying stably stratified turbulence', *J. Phys. Oceanogr.*, **24**, 2353–2386 (1994).
16. E.D. Skillingstad and D.W. Denbo, 'The role of internal gravity waves in the equatorial current system', *J. Phys. Oceanogr.*, **24**, 2093–2110 (1994).
17. K.B. Winters, P.N. Lombard, J.J. Riley and E.A. D'Asaro, 'Available potential energy and mixing in stratified fluids', *J. Fluid Mech.*, **289**, 115–128 (1995).
18. H. Michallet and G.N. Ivey, 'Experiments on mixing due to internal solitary waves breaking on uniform slopes', *J. Geophys. Res.*, **104**, 13 467–13 477 (1998).
19. G. Karniadakis, M. Israeli and S. Orszag, 'High-order splitting methods for the incompressible Navier–Stokes equations', *J. Comput. Phys.*, **97**, 414–443 (1991).